



Boosting CO₂ hydrogenation of Fe-based monolithic catalysts via 3D printing technology-induced heat/mass-transfer enhancements

Yang Wang^a, Shiyuan Lin^a, Meng Li^a, Chuanyong Zhu^a, Hao Yang^a, Pei Dong^a, Mingjie Lu^a,
Wenhang Wang^b, Jianlin Cao^a, Qiang Liu^c, Xiang Feng^a, Han Hu^a, Noritatsu Tsubaki^{b,*},
Mingbo Wu^a

^a College of New Energy, College of Chemistry and Chemical Engineering, State Key Laboratory of Heavy Oil Processing, China University of Petroleum (East China), Qingdao 266580, China

^b Department of Applied Chemistry, Graduate School of Engineering, University of Toyama, Gofuku 3190, Toyama 930-8555, Japan

^c National Engineering Research Center of Coal Gasification and Coal-Based Advanced Materials, Shandong Energy Group Co., Ltd., Jinan 250014, China

ARTICLE INFO

Keywords:

3D printing
CO₂ hydrogenation
Light olefins
Mass/heat-transfer enhancements
Reaction mechanism

ABSTRACT

The direct transformation of CO₂ into valuable chemicals with the aid of sustainable energy-generated H₂ has attracted enormous interest owing to the integrated functions of carbon elimination and non-fossil fuel-derived products supply. As one of the most promising catalysts for CO₂ hydrogenation, the chemical properties of Fe-based catalysts, such as electronic structure and coordination environment, have been widely studied. However, the mass/heat transfer effects in Fe-based catalysts are also crucial to the targeted product selectivity and catalytic stability, but have been rarely investigated due to the lack of facile fabrication protocols. Herein, we precisely fabricate and tailor the architecture of the Fe-based monolithic catalysts by a direct ink writing (DIW)-type three-dimensional (3D) printing technology under the guidance of the computationally controlled printing procedure. The Fe-based monolithic catalyst with spiral-type architecture delivers extremely high light olefins selectivity (52.6%) and space time yield (STY, 451.8 g_{CH₂} kg_{cat}⁻¹ h⁻¹) from CO₂ hydrogenation. Based on the mass-transfer simulation, the spiral-structured channels in the Fe-based monolithic catalyst lower the coverage of intermediates and products on the catalytic interface due to the optimal mass-transfer effect, thus maximizing the utilization of active sites and timely terminating the carbon-chain growth. More in-depth, the density functional theoretical (DFT) simulations verify that the relatively electron-rich catalytic interface with low intermediate coverage could facilitate the desorption of olefins and decelerate the C-C coupling step, which synergistically guarantee the enhanced light olefins synthesis performance. Furthermore, the enhanced heat-transfer effect endowed by the 3D architecture prolongs the life-time of catalyst by avoiding undesirable active site aggregation and carbon deposition. The powerful strategy for catalyst fabrication not only provides a new concept of regulating the CO₂ hydrogenation performance of Fe-based catalysts but also holds a great promise to spread into other catalytic systems for targeted synthesis.

1. Introduction

In addition to its greenhouse effect, CO₂ can also be employed as an abundant carbon resource for valuable chemicals synthesis[1,2]. The capture of CO₂ from the emission units and the following transformation into value-added chemicals not only represent a promising avenue to achieve carbon neutrality but also provide plenty of alternative routes for non-fossil fuel-based products synthesis[3,4]. In this respect, the hydrogenation of CO₂ with the assistance of sustainable energy-supplied

H₂ into various chemicals, such as methanol, light olefins, aromatics, etc., has attracted wide attention from industry and academia due to its high efficiency for targeted product synthesis and industrial applicability[5–7]. The practical application of CO₂ hydrogenation heavily relies on the rational design of heterogeneous catalysts with high capabilities of C-O bond activation and C-C bond coupling, as well as excellent long-term stability.

Fe-based catalysts have emerged as ideal candidates for C₂₊ products formation from CO₂ hydrogenation due to the co-existence of iron oxide

* Corresponding author.

E-mail address: tsubaki@eng.u-toyama.ac.jp (N. Tsubaki).

<https://doi.org/10.1016/j.apcatb.2023.123211>

Received 8 June 2023; Received in revised form 12 August 2023; Accepted 22 August 2023

Available online 26 August 2023

0926-3373/© 2023 Elsevier B.V. All rights reserved.

phase (mainly Fe_3O_4) for reverse water-gas shift reaction (RWGS, $\text{CO}_2 + \text{H}_2 \rightarrow \text{CO} + \text{H}_2\text{O}$) and iron carbide phase (mainly Fe_5C_2) for carbon-chain growth that following the Fischer-Tropsch synthesis (FTS) mechanism[8,9]. More importantly, the Fe-based catalysts can be combined with the second catalytic component (mainly zeolites) to convert $\text{CO}_2 + \text{H}_2$ into light olefins, ethanol, aromatics, etc. in a single-pass[10–14]. Therefore, the successive efforts on Fe-based catalysts design hold great potential to broaden the CO_2 hydrogenation reaction networks for valuable chemicals synthesis. Until now, much progress has been made to optimize the targeted products synthesis of Fe-based catalysts from CO_2 hydrogenation[15–18]. For instance, alkali metal modification has been recognized as a powerful strategy to enrich the electron density of Fe-based catalysts, by which the electron-rich alkenes dominate the products due to their rapid desorption from the catalytic interface. The existence of alkali metal is also beneficial to facilitate the carburization of Fe species, which in turn reinforces the carbon-chain propagation for long-chain hydrocarbons formation on iron carbide sites[19–22]. Additionally, the introduction of a second transition metal, e.g., Co, Mn, Cu, or Zn, was also widely employed to optimize the catalytic performance of Fe-based catalysts by tailoring the carbide phase composition and electronic structure[23–27]. Even though excessive attention has been paid to the rational design of Fe-based catalysts at nanoscale, such as the electronic structure and coordination environment of the active sites, the micron-scale architecture, as another key factor affecting their catalytic performance, is always neglected. Furthermore, the inferior long-term stability of the Fe-based catalyst stem from the active site aggregation during the high-temperature CO_2 hydrogenation process is also remain to be solved.

The influence mechanism of Fe-based catalyst architecture on the catalytic performance initially lies in the variation of mass and heat-transfer effects, which can be divided into the following aspects. On the one hand, the mass-transfer effect in the heterogeneous catalyst could change the coverage of intermediates and products on the catalytic interface[28–30]. In terms of CO_2 hydrogenation reaction catalyzed by Fe-based catalysts through the modified FTS pathway, the change of intermediates/products coverage induced by the mass transfer effect is not only conducive to the catalytic activity by altering the active site utilization efficiency but also responsible to the targeted product selectivity due to the variation of intermediates $-\text{C}_m\text{H}_n^*$ density on the catalytic interface for the carbon-chain propagation[31–36]. Therefore, the architecture-derived mass-transfer effect in the Fe-based catalysts can be employed as a powerful strategy to break the Anderson-Shultz-Flory (ASF) product distribution of the traditional FTS process. On the other hand, the architecture-enhanced heat-transfer effect in the Fe-based catalysts could suppress the undesirable active site aggregation and carbon deposition phenomena, which have been recognized as the main causes of the deactivation of Fe-based catalysts during CO_2 hydrogenation[37,38]. It should be noted that due to the exothermic property, the iron carbide-catalyzed carbon-chain growth process is more dependent on the architecture-enhanced heat-transfer effect of the Fe-based catalysts.

As mentioned above, the architecture-induced mass/heat-transfer effects are undoubtedly essential factors that regulate the CO_2 hydrogenation performance of Fe-based catalysts, especially the product selectivity and catalytic stability. However, due to the lack of facile protocols to precisely tailor the architecture of the Fe-based catalysts, the relationship between the architecture of Fe-based catalysts and the CO_2 hydrogenation performance is still unclear. Inspired by our previous work that integrates a couple of functions, such as catalytic sites and reaction field, into a self-catalytic reactor (SCR), three-dimensional (3D) printing technology might shed new light on the precise control of the architecture of Fe-based catalysts as demand[39]. As a versatile additive manufacturing technology, 3D printing possesses the advantage of high degree of freedom in structure design under the guidance of computational program[40–47]. In this context, we fabricate and tailor the architecture of Fe-based catalysts at the micron-scale by a direct ink

writing (DIW)-type 3D printing technique. Benefiting from the 3D printing-induced mass/heat transfer enhancements, the Fe-based catalyst with spiral-structure exhibits excellent long-term stability under high reaction temperature and pressure as well as extremely high selectivity (52.6%) and space time yield (STY, $451.8 \text{ g}_{\text{CH}_2} \text{ kg}_{\text{Fe@C}}^{-1} \text{ h}^{-1}$) of light olefins. The light olefins dominated in the products are important building blocks in the polymer industry, and the non-fossil fuel route for light olefins synthesis is promising to pursue the goal of sustainable development. The structure-function relationships in the monolithic Fe-based catalysts are clarified in detail by cooperating with the catalytic results, advanced characterizations, and simulations of mass/heat transfer processes and molecular-level reaction mechanisms. To the best of our knowledge, this is the first work to investigate the effect of Fe-based catalyst architecture on the targeted product selectivity and catalytic stability of CO_2 hydrogenation with the help of DIW-type 3D printing technology. The architecture-induced mass/heat-transfer effects are meaningful for the practical application of Fe-based catalysts in the CO_2 hydrogenation process. Furthermore, the ingenious catalytic performance tailoring strategy proposed in this work is also applicable to the syngas conversion, and is promising to spread into other catalytic reactions for oriented synthesis.

2. Experimental section

2.1. Catalyst preparation

2.1.1. Materials and chemicals

Ferric nitrate nonahydrate ($\text{Fe}(\text{NO}_3)_3 \cdot 9 \text{H}_2\text{O}$), triethylenediamine, 1,4-benzenedicarboxylic acid, dimethyl formamide (DMF), polyacrylonitrile (PAN), bentonite, hydroxypropyl methylcellulose (HPMC), and sodium carbonate (Na_2CO_3) that purchased from Shanghai Aladdin Biochemical Technology Co., Ltd. were of analytical grade and used without further purification. The deionized water used for catalyst preparation with a resistivity of 18.2 megohms was prepared using an ultrapure water system.

2.1.2. Synthesis of Na-Fe@C Catalyst

First, the Fe-based metal-organic frameworks (Fe-MOFs) were prepared by a hydrothermal method as reported in our previous work[22]. Typically, ferric nitrate nonahydrate (4.0 mmol, 1.62 g) and triethylenediamine (2.0 mmol, 0.22 g) were dissolved in DMF of 50 mL under vigorous stirring for 30 min. Then a DMF solution of 10 mL containing 1, 4-benzenedicarboxylic acid (0.70 g, 4.2 mmol) was added to the above solution dropwise. After stirring for 20 min, the mixture was transferred into a Teflon-lined autoclave (80 mL) and kept at 120°C for 24 h. The brown crystalline products were collected by centrifugation, followed by washing with deionized water five times and drying at 60°C in an oven overnight. The Fe-based catalyst was obtained by pyrolyzing the Fe-MOFs at 550°C for 3 h under a N_2 atmosphere with a heating rate of $5^\circ\text{C}/\text{min}$. The Fe-MOFs-derived catalyst was denoted as Fe@C. Alkali metal Na with the weight ratio of 3% was doped onto Fe@C by impregnation method with Na_2CO_3 as the Na source. The obtained catalyst was denoted as Na-Fe@C.

2.1.3. Preparation of the 3D-printed monolithic catalysts

The Fe-based monolithic catalysts were fabricated through the direct ink writing (DIW)-type three-dimensional (3D) printing technology with different binders (PAN or bentonite). For PAN as the binder of 3D-printed monolith, to make the desired printing ink, the Fe@C powders and PAN were first mixed by an agate mortar. Then, the sufficient amount of DMF and plasticizer HPMC was added into the mixture to obtain the homogeneous slurry with extrudable viscosity by the help of agate mortar. In the next step, the paste was transferred into a planetary mixer (Thinky, AGE-310) and mixed at 2000 rpm for 15 min. After further mixing, the printing ink with optimal viscosity and homogeneity was obtained. The printing ink was then transferred into a 5 cm^3 syringe

furnished with a 350–400 μm nozzle carefully. The fabrication of the monolith was performed on a lab-scale 3D printer (3D Bio-Architect® Sparrow, Regenovo Biotechnology Co., Ltd.), and the printing program was designed and coded by the 3D-Architect in advance software. All the 3D printing was performed at room temperature. After printing, the monoliths were washed by deionized water for 3–5 times and dried at 60 °C in an oven for 8 h. Due to the rapid curing property of PAN when it encountered H_2O , the monoliths became solid immediately after washing by H_2O , thus avoiding the collapse and cracking during the following drying and carbonization step. Then the monoliths were carbonized (550 °C for 3 h) in a tube furnace under a N_2 atmosphere with a heating rate of 5 °C/min. It should be noted that the active component Fe@C in each catalyst for the reaction test was kept at 0.1 g by controlling the total weight of the monolith. Monoliths with different configurations were fabricated. For the monolith with straight channels, all layers were stacked on top of each other. To fabricate the staggered channels, the printing layers were shifted to block the channels in the gas flow direction. The monolith with spiral channels was constructed by rotating layer-by-layer with the rotation angle set to 45°. The overall size of the monolithic catalyst as well as the wall thickness and channel size could be easily controlled by the nozzle size and the computational program. The representative cylinder structure with a diameter of ~12 mm and height of ~8 mm was employed to match the reactor for the catalytic reaction test. Alkali metal Na with the weight ratio of 3% was doped onto the obtained 3D printed monoliths by impregnation method with Na_2CO_3 as the Na source. The obtained 3D printed monoliths with different configurations were denoted as Na-Fe@C-3D-sta, Na-Fe@C-3D-str, and Na-Fe@C-3D-spi, where sta, str, and spi represent the staggered, straight, and spiral channels in the monoliths, respectively (Fig. 1a-c).

For the 3D-printed monolith with bentonite as the binder, to make the desired printing ink, the Fe@C, bentonite, and HPMC were mixed rigorously by an agate mortar, resulting in a homogeneous mixture. In the next step, the powder mixture and the solution were mixed and transferred to a planetary mixer and mixed at 2000 rpm for 15 min. After mixing, the printing ink with optimal viscosity and homogeneity was obtained. The 3D printing process was the same as that described

above. Only one configuration with spiral channels was constructed in the case with bentonite as the binder. After printing, the monolith was transferred into liquid nitrogen, and then freeze-drying was performed in a vacuum freeze dryer (LGJ-10E, Four-Ring Science Instrument Plant Beijing Co., Ltd.) for 24 h under vacuum condition. The temperature of the cold trap was set at -60 °C. Then the monolith was treated in a tube furnace, and the treatment conditions were similar to that for PAN-derived monolith. Alkali metal Na with the weight ratio of 3% was doped onto the obtained 3D printed monoliths by impregnation method with Na_2CO_3 as the Na source. The obtained spiral channel-type monolith with bentonite as the binder was denoted as Na-Fe@C-3D-B.

3D printing catalysts typically require binder to bond the catalyst into a monolith during post-processing without collapsing and cracking. PAN and bentonite are both suitable binders in 3D printing ink, after post-processing, they will be transformed into carriers for the monolithic catalysts (Bentonite was sintered, and PAN was carbonized into carbon carrier). 3D printing ink requires appropriate rheological properties, which have flow ability during extrusion and restore viscosity quickly to maintain its shape on the printing bed after extrusion. HPMC is a frequently-used plasticizer that can increase ink viscosity and endow ink with suitable rheological properties.

The non-3D printed catalyst was also prepared by directly carbonizing the printing ink, and the carbonization conditions were similar to that for the 3D printed monolith. Two types of non-3D printing catalysts were employed, the powder mode and the pellet mode. The pellet mode was fabricated by crushing and sieving the carbonized printing ink to 20–40 mesh. Alkali metal Na with the weight ratio of 3% was doped onto the obtained 3D printed monoliths by impregnation method with Na_2CO_3 as the Na source. The non-3D printed catalysts with two different macroscopic forms were denoted as Na-Fe@C-powder and Na-Fe@C-pellet, respectively.

2.2. Catalyst characterizations

2.2.1. Viscosity measurement

The viscosity of the printing ink was tested on a rheometer (HAKKE MARS, Thermo Scientific). The modulus was measured at a constant frequency of 1 Hz using an oscillating logarithmic stress scan (10^{-1} – 10^3 Pa), and the apparent viscosity was recorded using a strain scan at shear rates from 0.1 to 1000 s^{-1} .

2.2.2. Mechanical strength measurement

The mechanical strength of the monoliths printed with different binders was measured by an electronic universal testing machine (SHIMADZU AG-X plus) with a 10 kN measuring cell at 0.4 mm min^{-1} . The average compressive strength was calculated from at least three independent tests.

2.2.3. Characterization methods

X-ray diffraction (XRD) analysis was performed using a Rigaku RINT 2400 X-ray diffractometer with Cu $\text{K}\alpha$ radiation. The specific surface area and pore size distribution of the catalysts were measured by a Micromeritics 3Flex 2 M P instrument. Prior to the measurement, the catalyst was degassed at 200 °C for 10 h. The specific surface area was calculated by the Brunauer-Emmett-Teller (BET) method, and the average pore size and pore volume were calculated based on the Barrett-Joyner-Halenda (BJH, mesopores) and the t-Plot (micropores) methods, respectively. The morphology of the obtained catalysts was observed by a scanning electron microscopy (SEM, Zeiss Genimi 300) equipped with an energy dispersive spectroscopy (EDS, Oxford Inca Energy X-max 50 X-ray EDS). Transmission electron microscopy (TEM, JEM-2100 F, JEOL) was employed to observe the particle size variation of Fe-based active sites, and an EDS (Oxford Inca Energy X-maxN 80 T X-ray EDS) was equipped to monitor the elemental distribution (EDS mapping). X-ray photoelectron spectra (XPS) were collected on a Thermo Fisher Scientific ESCALAB 250Xi multifunctional spectroscopy. The ^{57}Fe

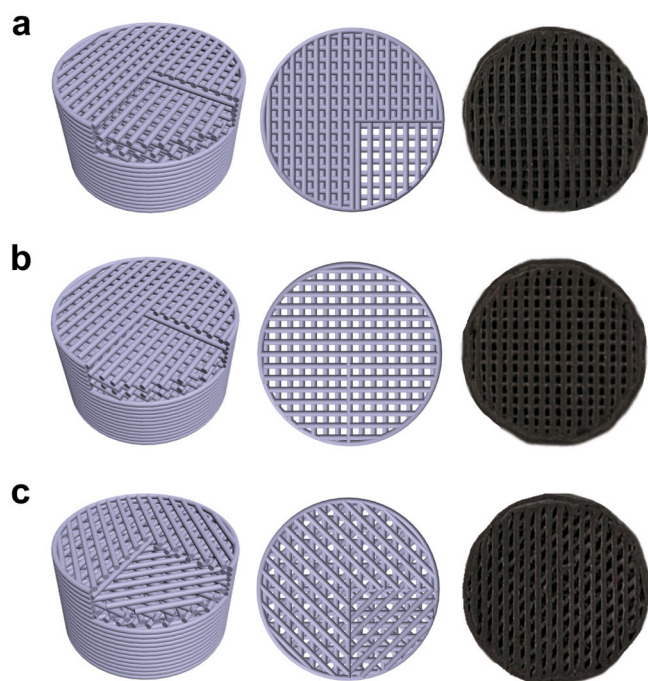


Fig. 1. The models and digital photographs (diameter of 12 mm) of the 3D printed Na-Fe@C-3D-sta (a), Na-Fe@C-3D-str (b), and Na-Fe@C-3D-spi (c).

Mössbauer spectra of the spent Na-Fe@C-pellet and Na-Fe@C-3D-spi catalyst were recorded at room temperature using a MFD-500AV (Topologic, Japan) spectrometer. The radioactive source was supplied by ^{57}Co (Rh) moving in a constant acceleration mode. The velocity was calibrated by a standard α iron foil. The components of the spent catalyst were identified based on the Mössbauer parameters, including isomer shift, quadruple splitting, and magnetic hyperfine field. Raman spectra of the catalysts were detected by a Raman spectrometer (InVia Raman Microscope, Renishaw).

2.3. Catalytic activity evaluation

The catalytic performance of the catalysts was measured in a fixed-bed reactor (Beijing ZXBLUE Co., Ltd.) with an internal diameter of 12 mm. Prior to the reaction, the catalyst was reduced by pure H_2 at 400°C for 4 h. After cooling down to the room temperature, the reactant gas (CO_2 hydrogenation: 24.3% CO_2 , 71.8% H_2 , and 3.9% Ar. Syngas conversion: 31.7% CO , 63.3% H_2 , and 5% Ar) was fed into the reactor until the pressure reached 3 MPa. At the same time, the temperature of the reactor was increased to 320°C . An ice trap ($\sim 0^\circ\text{C}$) set between the reactor and the back pressure valve was employed to collect the heavy hydrocarbons. The exhaust gas was analyzed by an online gas chromatograph (Fuli 9790II, Zhejiang Fuli Analytical Instruments Co., Ltd.) equipped with two detectors (thermal conductivity detector (TCD) and flame ionization detector (FID)). The TCD was connected to the TDX-01 (60–80 mesh, 3 mm \times 2 m) and Porapak-Q (60–80 mesh, 3 mm \times 1 m) packed columns for the analysis of Ar, CO , CH_4 , and CO_2 , and the FID was connected to the HP-PLOT/Q capillary column (0.53 mm \times 30 m) to detect gas-phase hydrocarbons. The heavy hydrocarbons collected by the ice trap were analyzed by an off-line gas chromatograph (GC9790II) equipped with an FID and an InerCap-5 capillary column (GL Sciences, 0.25 mm \times 30 m). CO_2 or CO (denoted as CO_x , $x = 1$ or 2) conversion and product selectivity were calculated by the following equations.

(1) CO_x conversion was calculated according to:

$$\text{CO}_x \text{ Conversion} = \frac{\text{CO}_{x\text{inlet}} - \text{CO}_{x\text{outlet}}}{\text{CO}_{x\text{inlet}}} \times 100\%$$

Where $\text{CO}_{x\text{inlet}}$ and $\text{CO}_{x\text{outlet}}$ represent moles of CO_x at the inlet and outlet, respectively.

(2) Product selectivity was calculated as the percentage of CO_x converted into a given product and according to:

$$\text{Sel}_i = \frac{N_i \times n_i}{\sum_i (N_i \times n_i)} \times 100\%$$

Where N_i and n_i represent the mole percentage and carbon number of product i .

(3) CO_x selectivity (CO selectivity for CO_2 hydrogenation and CO_2 selectivity for syngas conversion) was calculated according to:

$$\text{CO selectivity} = \frac{\text{CO}_{\text{outlet}}}{\text{CO}_{2\text{inlet}} - \text{CO}_{2\text{outlet}}} \times 100\%$$

$$\text{CO}_2 \text{ selectivity} = \frac{\text{CO}_{2\text{outlet}}}{\text{CO}_{\text{inlet}} - \text{CO}_{\text{outlet}}} \times 100\%$$

The carbon balances of the reaction data were calculated, which were all higher than 90%. Typically, the experimental data after the reaction of 24 h were used for discussion. For CO_2 (or syngas) conversion, the total selectivity of CO (or CO_2) and hydrocarbon was set at 100%.

2.4. Simulations

2.4.1. Computational fluid dynamics simulation

In order to investigate the flow diffusion phenomena and heat-transfer effects in the monolithic catalysts with different

configurations, computational fluid dynamic (CFD) simulations were carried out using COMSOL Multiphysics® software. The details of CFD simulations are provided in Supporting Information.

2.4.2. Density functional theory calculation

All the computational calculations were carried out in the framework of the density functional theory (DFT) with the projector augmented plane-wave method, as implemented in the Vienna ab initio simulation package (VASP)[48,49]. The generalized gradient approximation proposed by Perdew, Burke, and Ernzerhof was employed for the exchange-correlation potential[50,51]. The cutoff energy for plane wave was set to 400 eV. Electron smearing was used via the Methfessel-Paxton technique with a smearing width consistent to $\sigma = 0.2$ eV. The adsorption energies included spin polarization. All transition states were searched by combining the climbing image nudged elastic band (CI-NEB) method with the dimer method, and the stretching frequencies of the saddle points were analyzed to ensure a transition state with only one imaginary frequency[52,53]. Bader charge analysis and charge density difference analyses were performed by using the code developed by Henkelman and co-workers[54,55]. And the VASPKIT code was used for the subsequent VASP calculation data results processing[56].

The adsorption energy (E_{ads}) was defined as the following equation

$$E_{\text{ads}} = E_{\text{X/slab}} - [E_{\text{slab}} + E_{\text{X}}]$$

where $E_{\text{X/slab}}$ is the total energy of the slab with adsorbates in its equilibrium geometry, E_{slab} is the total energy of the bare slab, and E_{X} is the total energy of the free adsorbates in the gas phase. Therefore, the more negative the E_{ads} , the stronger the adsorption.

The reaction energy (ΔE) and barrier (E_{act}) were calculated via the following equations

$$\Delta E = E_{\text{FS}} - E_{\text{IS}}$$

$$E_{\text{act}} = E_{\text{TS}} - E_{\text{IS}}$$

where E_{IS} , E_{TS} , and E_{FS} are the total energy of the corresponding initial state (IS), transitional state (TS), and final state (FS), respectively.

The calculated Fe_5C_2 cell is a monoclinic crystal and shows a C2/c crystallographic symmetry including 20 Fe and 8 C atoms per unit cell. Its lattice parameters are $a = 11.56 \text{ \AA}$, $b = 4.51 \text{ \AA}$, $c = 4.99 \text{ \AA}$, and $\beta = 97.67^\circ$, which are consistent with the experimental and theoretical results[57]. The $\text{Fe}_5\text{C}_2(510)$ surface size of $p(2 \times 2)$ with 3 layers was used to model the catalyst surface. The vacuum thickness of 10 \AA was employed to avoid the interactions between the slabs. The all layers and adsorbates were allowed to relax. A K-point grid of $2 \times 2 \times 1$ was selected. All structures were optimized until the forces on the atoms were less than 0.03 eV/\AA . The transition state structure was optimized until the forces on atom become converged to 0.05 eV/\AA . The top and

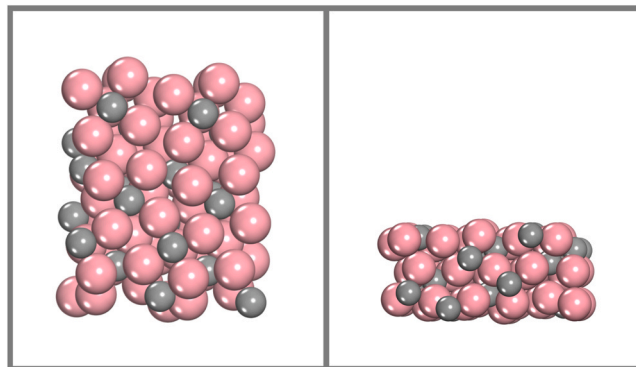


Fig. 2. The top (left) and side (right) view structures of $\text{Fe}_5\text{C}_2(510)$ (Fe atoms in pink, C atoms in grey, and H atoms in white).

side views of the studied χ -Fe₅C₂ (510) surface are illustrated in Fig. 2.

3. Results and discussion

3.1. Fabrication of Fe-based monolithic catalysts via three dimensional (3D) printing technology

The fabrication procedures of Fe-based monolithic catalysts via direct ink writing (DIW)-type three-dimensional (3D) printing are illustrated in Scheme 1. After mixing by a planetary mixer, the rheological behavior of the printing ink was studied. The viscosity of the printing ink decreased with the shear rates increasing (Fig. 3a), which implies the typical shear-thinning non-Newtonian fluid behavior [58, 59]. As shown in Fig. 3b, under low shear stress (< 200 Pa), the storage modules (G') were nearly an order of magnitude higher than that of loss modules (G''), which guarantees the stable flow of ink during the extrusion process. With the increase of shear stress that corresponding to the step of ink extrusion through a nozzle, G'' played a dominating role, indicating that the printing ink could be smoothly extruded from the fine nozzle. When the printing ink was extruded from the nozzle to the substrate, the high G' value was beneficial for the shape retention of the printed 3D architectures.

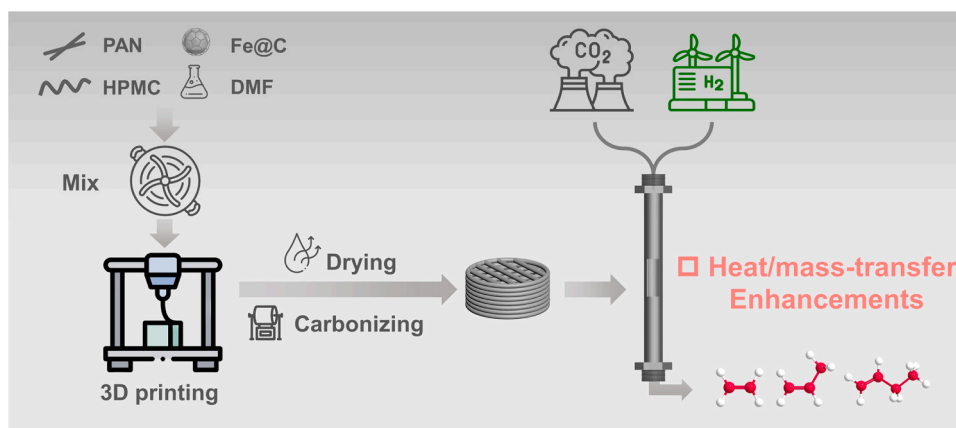
The extruded filaments were assembled into desired architectures under the guidance of a computational program. Three kinds of Fe-based monolithic catalysts with straight, spiral, and staggered channels were successfully fabricated (Fig. 1a-c). Due to the rapid curing property of PAN when it encountered H₂O, the stabilization process was realized by immersing the structured ink into H₂O, which is more time-saving than the traditional freeze-drying strategy [60,61]. To transform the organic precursors, such as HPMC and PAN, into carbon species and further stabilize the monolithic catalysts, carbonization treatment at 550 °C under an inert N₂ atmosphere was performed. No obvious structural shrinkage was detected after drying and carbonization treatments of the monolithic catalysts. As shown in the scanning electron microscopy (SEM, Fig. 4) images, the filament diameter and the distance between the adjacent filaments in the obtained Fe-based monolithic catalysts were maintained at around 350 and 500 μ m, respectively, which are almost similar to the data used in the computational program. At last, the alkali metal Na species with weight ratio of 3% was doped onto the Fe-based catalysts to tailor their electronic properties.

After the 3D printing process, the specific surface area of the catalyst decreased due to the encapsulation of the active components by the binder (Table S1). As one of the critical criteria for the practical application, the mechanical strength of the 3D-printed monolithic catalysts was evaluated (Fig. 5 and Table S2). Na-Fe@C-3D-spi exhibited high compressive strength of 1.6 MPa with the strain at the time of fracture keeping at 5%. The Young's modulus of Na-Fe@C-3D-spi that calculated

from the slope of stress-strain curve was as high as 33.0 MPa. For comparison, the monolithic catalyst with spiral channels was also fabricated with bentonite as the binder (denoted as Na-Fe@C-3D-B), which has been widely employed to assemble the zeolitic materials via 3D printing technology. However, the compressive strength and Young's modulus of Na-Fe@C-3D-B were only 0.36 and 2.5 MPa, respectively, which are both much lower than that of Na-Fe@C-3D-spi. Therefore, in addition to avoiding tedious freeze-drying treatment, the choice of PAN as the 3D printing binder can also enhance the mechanical strength of the Fe-based monolithic catalyst.

The heat/mass-transfer effects endowed by the micron-scale channels between the printed filaments were estimated by computational fluid dynamics (CFD) simulations using COMSOL Multiphysics® software. The geometric models of Na-Fe@C-3D-sta, Na-Fe@C-3D-str, Na-Fe@C-3D-spi are shown as Fig. 6a-c. The size and structure of the models were consistent with the actual catalysts. For Na-Fe@C-3D-str, every layer was stacked directly with the rotation angle of 90°. For Na-Fe@C-3D-sta, the middle layer of every three layers was shifted to block the channels in the gas flow direction. For Na-Fe@C-3D-spi, each layer was stacked with the rotation angle of 45°. First, the gas flow diffusion phenomena in the channels of different monoliths were simulated with a mixture of CO₂/H₂ as the representative flow media. The staggered filaments endowed zigzag channels in Na-Fe@C-3D-sta, in which the mass-transfer process was limited due to the blocked channels. Therefore, as demonstrated in Figs. 6d and 6g, Na-Fe@C-3D-sta monolithic catalyst delivered the minimum CFD simulated flow rate of 0.051 m s⁻¹ and maximum pressure drop of 0.850 Pa. Na-Fe@C-3D-str with straight channels undoubtedly guaranteed the unimpeded gas diffusion process with the faster flow rate of 0.053 m s⁻¹ as shown in Fig. 6e. Due to the existence of intersecting channels, the lowest pressure drop of 0.828 Pa was obtained from the Na-Fe@C-3D-str monolith (Fig. 6h). For the Na-Fe@C-3D-spi catalyst, even though the spiral architecture fabricated by the rotation of each 3D printing layer prolonged the gas flow diffusion pathway, the flexural but unblocked channels could change the laminar flow into the turbulent mode, therefore enhancing the mass-transfer effect. Quantitatively, the CFD simulated flow rate in Na-Fe@C-3D-spi maintained at the highest level of 0.059 m s⁻¹ accompanied with the moderate pressure drop of 0.839 Pa (Figs. 6f and 6i).

Furthermore, the heat transfer effects in the different monolithic catalysts were also evaluated, and the simulated temperature fields are illustrated in Fig. 6j-l. Even though the range of temperature change obtained from the three architectures was very close, distinctly diverse high-temperature fields were distributed on the different monoliths. Na-Fe@C-3D-spi exhibited a significantly smaller high-temperature region (dark red region) due to the fast heat-transfer effect in the spiral channels. For the CO₂ hydrogenation reaction, the hot spot formed in the



Scheme 1. Schematic illustration for the fabrication of Fe-based monolithic catalysts via 3D printing technology.

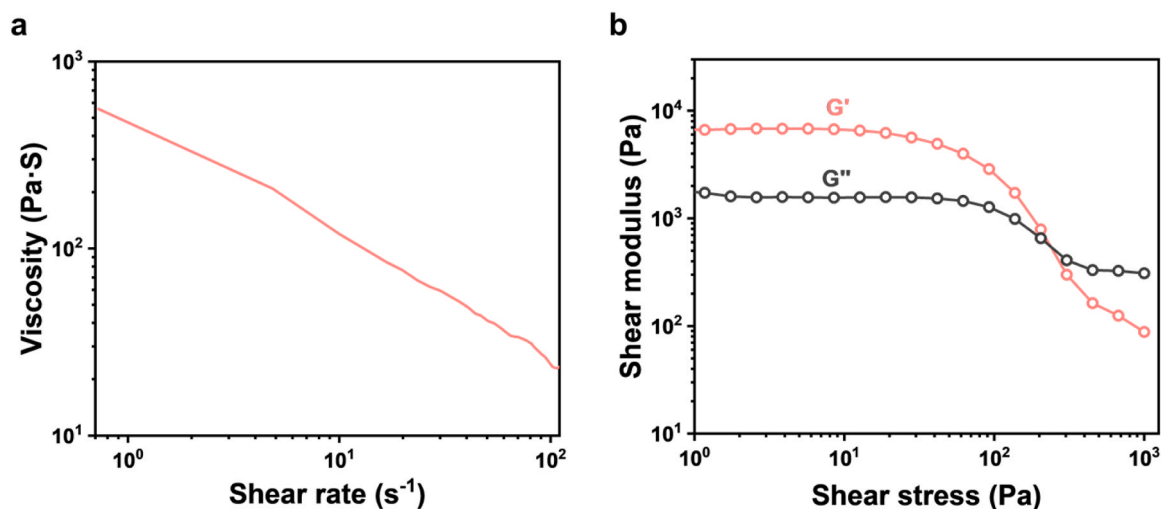


Fig. 3. (a) Rheological behavior of PAN-based ink. (b) The storage (G') and loss (G'') modulus of PAN-based ink as a function of shear stress.

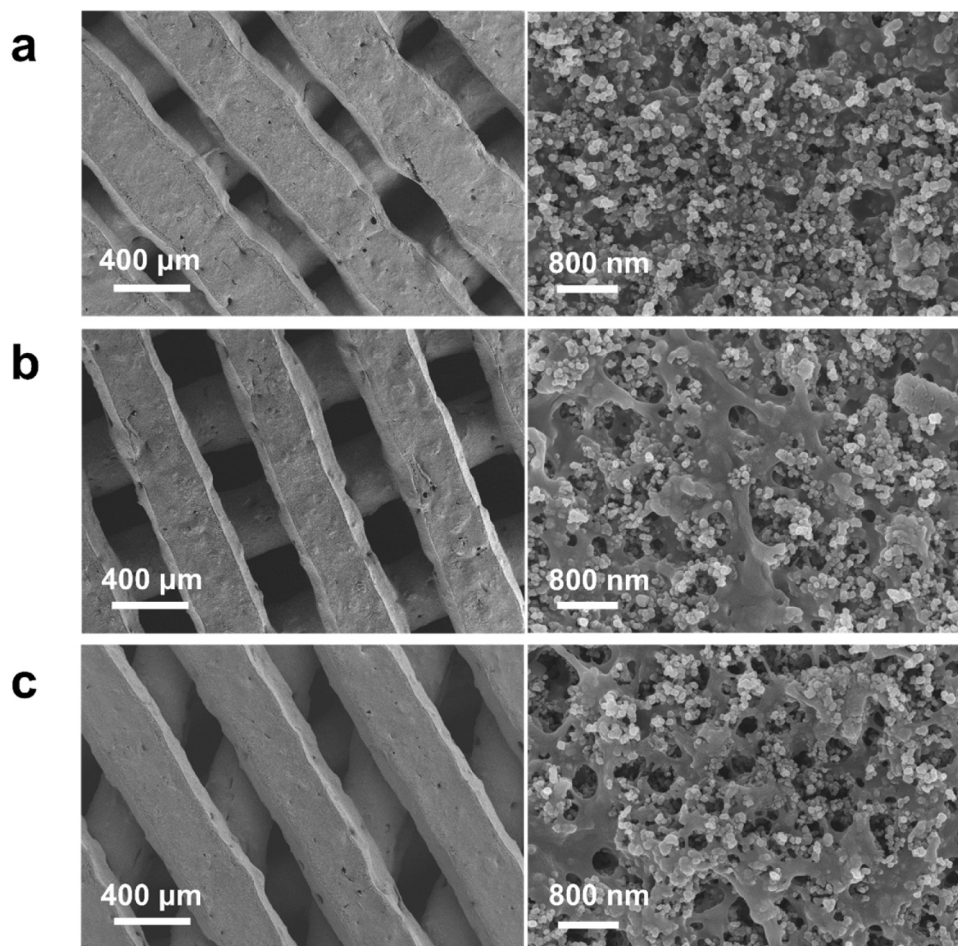


Fig. 4. Low and high-magnification SEM images of the 3D printed Na-Fe@C-3D-sta (a), Na-Fe@C-3D-str (b), and Na-Fe@C-3D-spi (c).

catalyst bed is the main cause of active sites aggregation and catalyst degradation. The excellent heat-transfer effect in Na-Fe@C-3D-spi is beneficial to avoid the undesirable sintering of Fe-based active sites and prolong the long-term stability of the catalyst, which will be discussed detailed in the following statement.

To investigate the difference in mass/heat transfer between 3D printing and non 3D printing catalysts, we conducted CFD simulation on

Na-Fe@C-pellet. We used irregularly arranged ellipsoids to represent catalyst particles, and other conditions were consistent with those of 3D printing catalysts. As shown in Fig. S1, Na-Fe@C-3D-pellet delivered a higher CFD simulated flow rate of 0.087 m s^{-1} and lower pressure drop of 0.365 Pa than 3D printing catalysts. However, the flow rate distribution in the catalyst is extremely uneven, with only a few areas achieving high flow rates, while more areas can only achieve lower flow

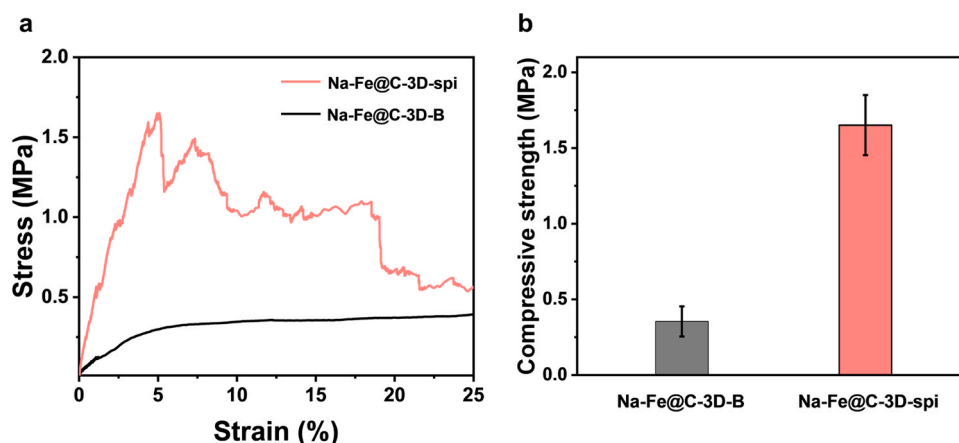


Fig. 5. (a) Representative stress-strain curves and (b) compressive strength of Na-Fe@C-3D-spi and Na-Fe@C-3D-B.

rates than 3D printed catalysts, which has a negative effect on mass transfer. On the other hand, due to the dense accumulation of catalyst pellets, the reaction heat is difficult to be released timely, resulting in much higher temperature than that of the 3D printing catalysts.

3.2. Structure-function relationship of Fe-based monolithic catalysts for CO₂ hydrogenation

The X-ray diffraction (XRD) pattern of the carbonized ink exhibited strong typical peaks at $2\theta = 30.1^\circ$, 35.4° , and 62.5° (Fig. S2), which corresponded well with the (220), (311), and (440) planes of Fe₃O₄ crystal phase (PDF #19-0629), respectively [14,22]. It is believable that the printing process has no effect on the crystal structure of the monolithic catalysts due to the physically extruded process under ambient conditions. Fe₃O₄ has been widely recognized as the active site for the reverse water-gas shift (RWGS, $\text{CO}_2 + \text{H}_2 \rightarrow \text{CO} + \text{H}_2\text{O}$) reaction, which is the initial step for CO₂ conversion through a modified Fischer-Tropsch synthesis (FTS) route. As shown in the high-magnification SEM images (Fig. 4) and energy dispersive spectra (EDS) (Fig. S3) mapping, the Fe-MOFs derived Fe@C nanoparticles with the diameter smaller than 100 nm were homogeneously dispersed on the carbon substrate that evolved from the carbonization of PAN binder. All of the 3D printed monolithic catalysts exhibited similar nanoscale architecture with carbon skeleton forming interconnected structure, which is favorable for the permeation of reactants to the active sites. It is obvious that the 3D printing program was decisive to the micron-scale configuration, while did not affect the nanoscale morphology.

The CO₂ hydrogenation reactions of the non-3D printed Na-Fe@C and 3D printed monolithic catalysts were performed under 320 °C and 3 MPa to investigate the effect of micron-scale architecture on the catalytic performance (Fig. 7 and Table S3). The non-3D printed catalyst with two different macroscopic forms (pellets of 20–40 mesh and powder) delivered markedly different catalytic performance. The powdered Na-Fe@C catalyst (denoted as Na-Fe@C-powder) exhibited an olefins selectivity of 49.5% at a CO₂ conversion of 24.9% with the ratio of olefins to paraffins (o/p) to be 1.9. For the pelleted Na-Fe@C catalyst (denoted as Na-Fe@C-pellet), the olefins selectivity, CO₂ conversion, and o/p ratio were increased to 55.8%, 29.1%, and 2.7, respectively. It is obvious that the discrepant micro-scale channels formed from the different catalyst forms (powder or pellet) have a significant influence on the catalytic performance, especially in the alkenes selectivity and CO₂ activation capacity, which inspired us to tailor the micron-scale architecture of the Fe-based catalysts to boost their CO₂ hydrogenation performance. Because of the influence of the binder, the CO₂ conversion of Na-Fe@C-powder and Na-Fe@C-pellet was lower than that of Na-Fe@C-without binder. However, benefiting from the monolithic structure, the 3D printing catalysts with additives achieved higher CO₂

conversion and light olefins (C₂–C₄) yield than that of Na-Fe@C-without binder, especially for Na-Fe@C-3D-str and Na-Fe@C-3D-spi.

Benefiting from their similar open channels constructed by 3D printing, all 3D printed catalysts achieved high selectivity for light olefins. Although they have similar selectivity for light olefins, we can further evaluate the differences in hydrogenation and carbon-chain growth between Na-Fe@C-3D-sta, Na-Fe@C-str, and Na-Fe@C-spi through o/p ratios and α value. For the Na-Fe@C-3D-sta catalyst, the olefins selectivity of 57.8% accompanied with the o/p ratio of 3.1 were achieved at a CO₂ conversion of 32.1%, which are all superior to the non-3D printed counterparts due to the enhanced mass-transfer effects endowed by the 3D printing technology. The mass-transfer effects were further optimized by precisely tuning the channels in Fe-based monolithic catalysts to spiral and straight types. The weaker mass-transfer resistances in Na-Fe@C-3D-str and Na-Fe@C-3D-spi guaranteed the distinguished olefins selectivity (60.2% and 60.9%, respectively), CO₂ conversion (39.0% and 38.5%, respectively), and o/p ratios (3.9 and 4.0, respectively). It is easy to understand the mass-transfer enhanced CO₂ conversion phenomenon, in which the rapid removal of products that adsorbed on the catalytic interface would feed up the active sites timely for the continuous activation of more CO₂ molecules. In terms of olefins selectivity, the o/p ratios obtained from the 3D printed catalysts were positively correlated with the CFD simulated flow rate (Fig. 8a), indicating that the enhanced mass-transfer process could clean the products out of the catalytic bed immediately to avoid the undesirable hydrogenation of the re-adsorbed olefins.

Regarding to the detailed product distribution, the architecture of the Fe-based monolithic catalyst is also susceptible to the carbon-chain growth probability, which indeed originates from the variation of mass-transfer effect. As illustrated in Fig. 8b, the correlation between the mass-transfer effect and the carbon-chain growth probability α value (Fig. 9) was established. With the enhancement of the mass-transfer effect as reflected by the increase of CFD simulated flow rate, the α value synchronously decreased owing to the timely termination of the carbon-chain growth. The surface carbene -CH₂* insertion mechanism has been widely accepted to explain the catalytic behaviors of FTS, in which the carbene -CH₂* species produced from the hydrogenation of -C* (from CO dissociation) act as monomers and initiators for carbon-chain growth [62–64]. Owing to the rapid desorption of reaction intermediates with the help of enhanced mass-transfer effect, the low coverage degree of -CH₂* species on the catalytic interface could decrease the probability of carbon-chain propagation, therefore shortening the carbon-chain length of the products. Na-Fe@C-3D-spi with the most optimal mass-transfer architecture boosted the synthesis of light hydrocarbons, especially of light olefins (C₂–C₄).

Based on the above discussion, the enhanced mass-transfer effect endowed by the tailorable 3D printing technology is essential to boost

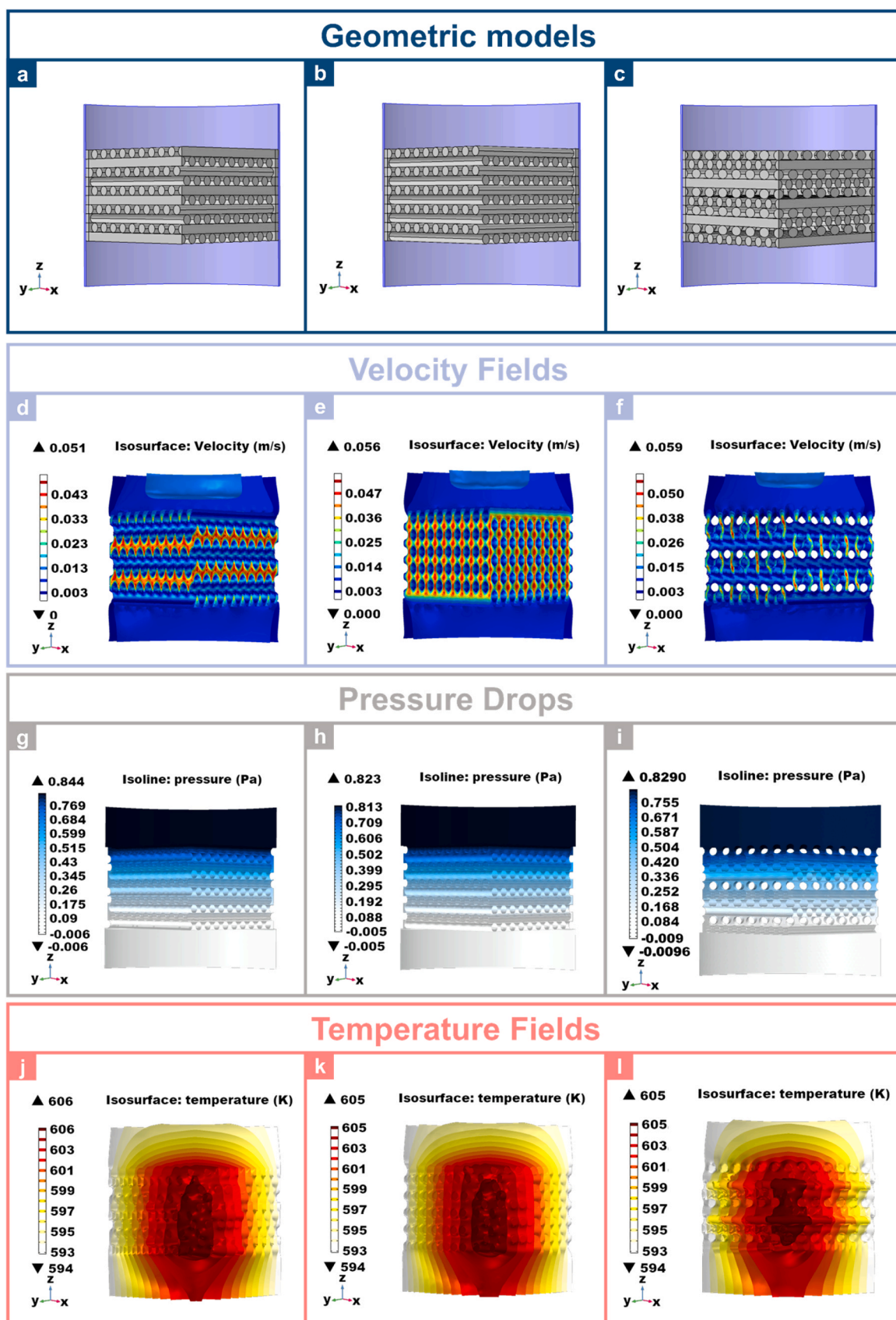


Fig. 6. Simulation of mass/heat transfer processes in monolithic catalysts. The CFD simulated geometric models (a-c), velocity fields (d-f), pressure drops (g-i), and temperature fields (j-l) in the 3D printed Na-Fe@C-3D-sta (a, d, g and j), Na-Fe@C-3D-str (b, e, h and k), and Na-Fe@C-3D-spi (c, f, i and l).

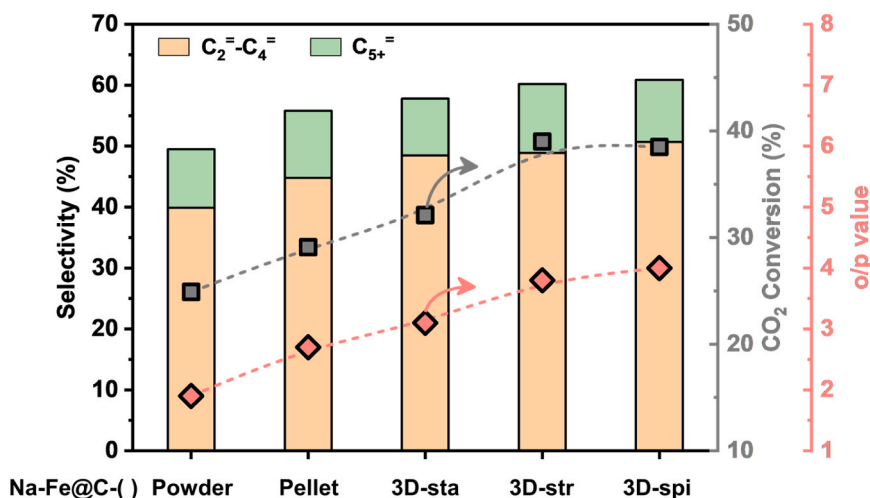


Fig. 7. Catalytic performance of the non-3D printed Na-Fe@C and 3D printed monolithic catalysts in CO₂ hydrogenation, reaction conditions: 320 °C, 3 MPa (24.3% CO₂, 71.8% H₂, and 3.9% Ar), 15 mL min⁻¹, Fe@C active component of 0.1 g in the catalyst bed, and time on stream (TOS) = 24 h.

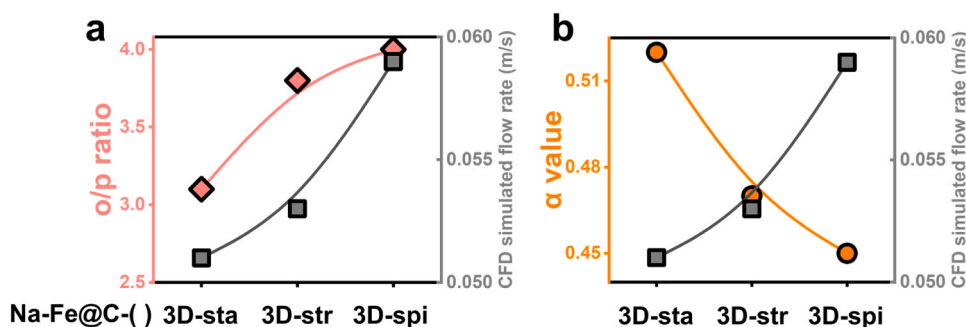


Fig. 8. (a) The relationship between the o/p ratio and CFD simulated flow rate. (b) The relationship between the mass-transfer effect and the carbon-chain growth probability α value.

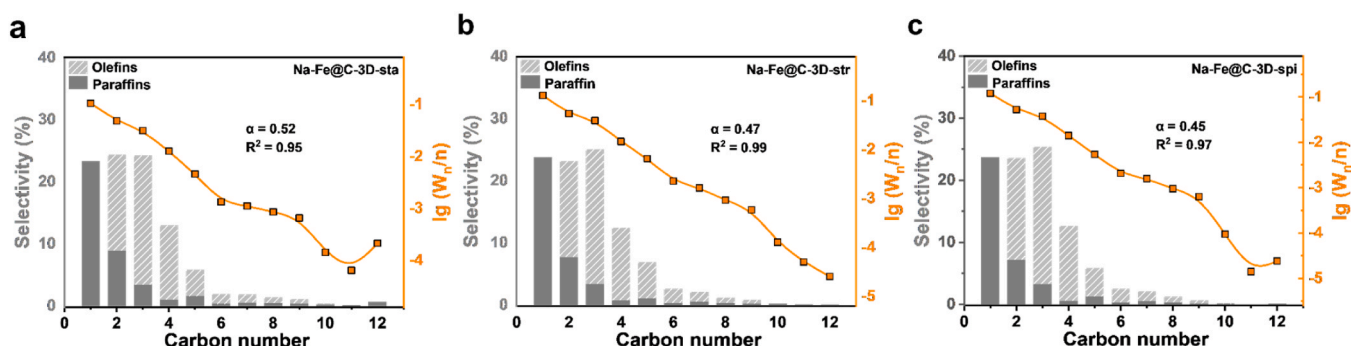


Fig. 9. The detailed product distribution and carbon-chain growth probability α value of Na-Fe@C-3D-sta (a), Na-Fe@C-3D-str (b), and Na-Fe@C-3D-spi (c) in CO₂ hydrogenation. R^2 is the coefficient of determination, describing the goodness of linear fitting. W_n is the weight fraction of the product with n carbon atoms.

light olefins synthesis by synergistically avoiding the overgrowth of carbon-chain and excessive hydrogenation of olefins. Comprehensively, the space time yield (STY) of C₂-C₄ achieved from Na-Fe@C-3D-str (225.5 g_{CH₂} kg_{Fe@C}⁻¹ h⁻¹) and Na-Fe@C-3D-spi (228.9 g_{CH₂} kg_{Fe@C}⁻¹ h⁻¹) with excellent mass-transfer phenomena obviously outperformed that of Na-Fe@C-powder (99.6 g_{CH₂} kg_{Fe@C}⁻¹ h⁻¹), Na-Fe@C-pellet (142.4 g_{CH₂} kg_{Fe@C}⁻¹ h⁻¹), and Na-Fe@C-3D-sta (181.3 g_{CH₂} kg_{Fe@C}⁻¹ h⁻¹) with relatively poor mass-transfer effects (Table S3 and Fig. S4). Moreover, the mass-transfer enhancement effect in boosting light olefins synthesis from CO₂ hydrogenation can be verified again by the comparative experiments on Na-Fe@C-3D-spi catalyst with varied gas hourly space

velocities (GHSV) (Fig. S5 and Table S4). Raising the gas flow rate resulted in the increase of olefins selectivity due to the facilitated desorption of olefins and timely termination of carbon-chain growth under strong gas flow turbulence, which is similar to the trends obtained in Fig. 8. Interestingly, the STY of light olefins (451.8 g_{CH₂} kg_{Fe@C}⁻¹ h⁻¹) obtained from the Na-Fe@C-3D-spi catalyst outperformed the most results reported in other literature (Fig. 10 and Table S5).

For the two different binders (PAN and bentonite), the 3D-printed catalysts Na-Fe@C-3D-spi (PAN as binder) and Na-Fe@C-3D-B (bentonite as binder) exhibited even similar specific surface area (Table S1), and sufficient mesopores ensured the accessibility of the

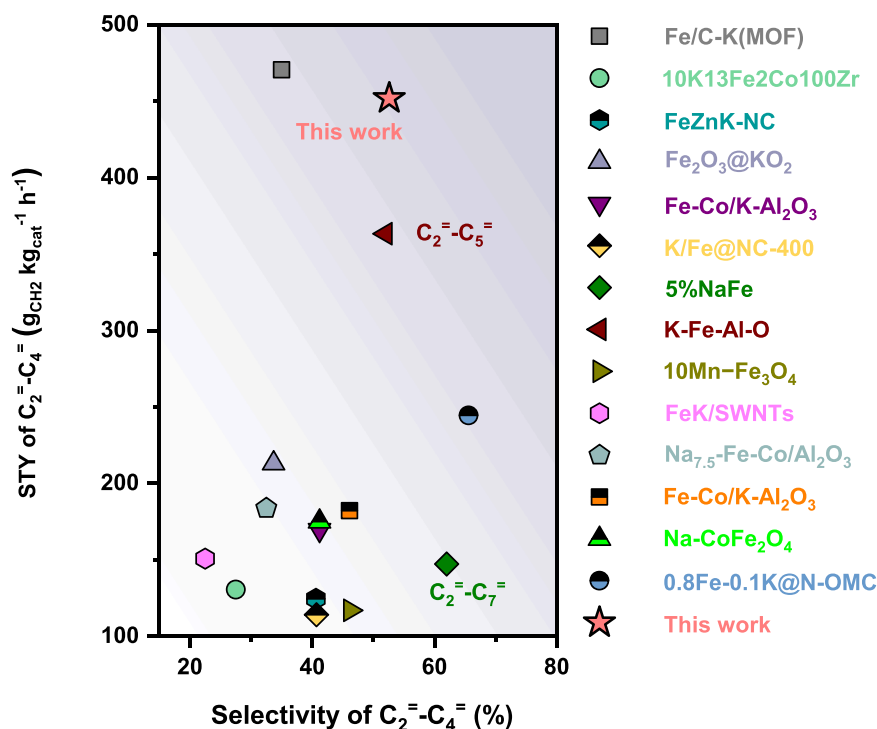


Fig. 10. Comparison of the light olefins (C_2-C_4) synthesis performance obtained from Na-Fe@C-3D-spi with the results reported in other literature (only the results with STY higher than $100 \text{ g}_{\text{CH}_2} \text{ kg}_{\text{cat}}^{-1} \text{ h}^{-1}$ were plotted in this figure, and detailed information see in Table S5).

active sites, so that their catalytic activities were not significantly inhibited (Table S3). However, Na-Fe@C-3D-spi is superior to Na-Fe@C-3D-B in terms of CO_2 conversion and C_2-C_4 selectivity, which can be attributed to the appropriate interaction between the active site and additives.

In addition to boosting the selectivity of light olefins, the 3D-printed architecture is also favorable to prolong the lifetime of the Fe-based active sites. Even though the Fe_5C_2 active phase for carbon-chain growth was appeared in the XRD patterns of all the spent Fe-based catalysts (Fig. S6), the different micro-scale architectures delivered

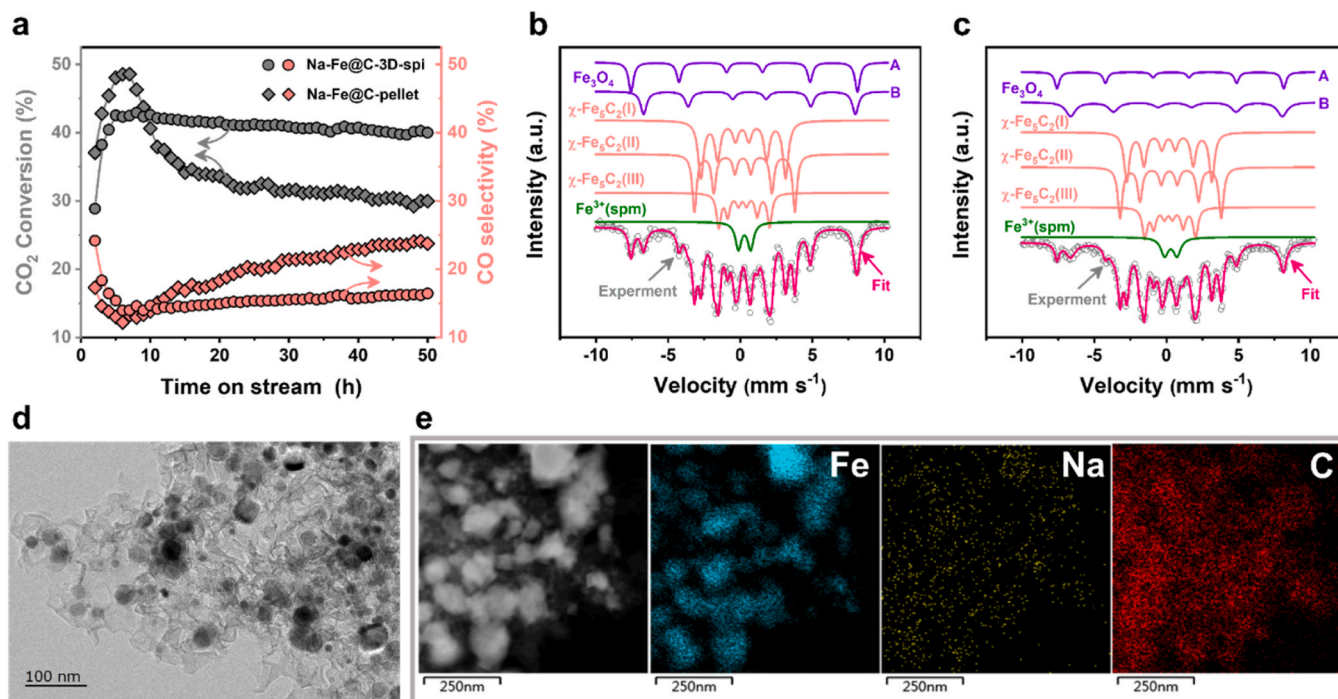


Fig. 11. (a) Long-term stability of non-3D printed Na-Fe@C-pellet and 3D printed Na-Fe@C-3D-spi in CO_2 hydrogenation, reaction conditions: 320°C , 3 MPa (24.3% CO_2 , 71.8% H_2 , and 3.9% Ar), 15 mL min^{-1} , Fe/C active component of 0.1 g in the catalyst bed, and time on stream (TOS) = 50 h. (b,c) ^{57}Fe Mössbauer spectra of the spent Na-Fe@C-3D-spi (b) and Na-Fe@C-pellet (c). (d) TEM image of the spent Na-Fe@C-3D-spi. (e) HAADF-STEM image and the corresponding elemental mapping images of Fe, Na, and C elements in the spent Na-Fe@C-3D-spi.

distinct reaction behaviors. With Na-Fe@C-3D-str, Na-Fe@C-3D-sta, Na-Fe@C-3D-spi, and the non-3D printed Na-Fe@C-pellet as representative examples, the relationship between the catalyst architecture and reaction stability was established. As shown in Fig. 11a, Fig. S7, and Table S6, at the initial stage of CO₂ hydrogenation reaction (first 8 h), all of the catalysts experienced a climbing process for CO₂ conversion, and Na-Fe@C-pellet exhibited a more sharply enhanced CO₂ activation capability. The induction period for CO₂ activation is originated from the carburization of Fe species by CO that produced by Fe₃O₄-catalyzed RWGS reaction, which can be confirmed by the decrease of CO selectivity at the initial stage. With the increase of iron carbide content in the Fe-based catalyst, the continuous consumption of CO via the iron carbide-catalyzed FTS could drive the tandem process forward, therefore boosting the CO₂ transformation capacity at the initial stage. Ideally, the CO₂ conversion rate tends to be constant due to the unchanged Fe₃O₄ and iron carbide contents in Fe-based catalyst. However, after the climbing process, a noticeable and continuous decrease of CO₂ conversion (from ~48% to ~30%) occurred on Na-Fe@C-3D-sta and Na-Fe@C-pellet, while Na-Fe@C-3D-str and Na-Fe@C-3D-spi maintained a high CO₂ transformation rate even after long-term stability test of 50 h. Accordingly, the CO selectivity from Na-Fe@C-3D-str and Na-Fe@C-3D-spi kept stable after the induction period, whereas Na-Fe@C-3D-sta and Na-Fe@C-pellet underwent a significant increase in CO selectivity during the long-term operation.

To illustrate the driving force of 3D printing technology in boosting the catalyst durability, multiple characterization of the spent Na-Fe@C-3D-spi and Na-Fe@C-pellet was performed. As shown in the X-ray photoelectron spectra (XPS) (Fig. S8), divalent Fe (Fe²⁺, Fe 2p_{3/2} at 710.7 eV and Fe 2p_{1/2} at 723.8 eV) and trivalent Fe (Fe³⁺, Fe 2p_{3/2} at 711.9 eV and Fe 2p_{1/2} at 725.0 eV) were detected in both of the spent Na-Fe@C-pellet and Na-Fe@C-3D-spi. Furthermore, the appearance of a weak XPS peak at around 707.2 eV that corresponding to the Fe-C bond confirmed the formation of iron carbides during the reaction, which is consistent with the XRD results[65]. More finely, four kinds of Fe-based active sites, Fe₃O₄, χ -Fe₅C₂, θ -Fe₃C, and Fe³⁺, were detected in the ⁵⁷Fe Mössbauer spectra of the spent catalysts (Figs. 11b and 11c). The contents of Fe₃O₄ (26.3% and 23.3%), χ -Fe₅C₂ (43.6% and 43.8%), θ -Fe₃C (22.8% and 25.6%), and Fe³⁺ (7.3% and 7.3%) in the spent Na-Fe@C-pellet and Na-Fe@C-3D-spi were at the similar level (Table S7). We further conducted Inductive Coupled Plasma Emission Spectrometer (ICP) on Na-Fe@C-pellet with different operation times (fresh, 24 h, and 50 h). The ICP testing shown that the Na content in the Na-Fe@C-3D-pellet catalysts with different operation times was very close (2.62 wt% for fresh catalyst, 2.60 wt% for catalyst after 24 h reaction, and 2.56 wt% for catalyst after 60 h reaction). Based on the XPS, Mössbauer, and ICP results, the variation of catalytic behaviors could not result from the subtle differences in the chemical composition of the spent catalysts.

The transmission electron microscopy (TEM) images of the spent catalysts illustrated that the Fe-based active sites in the Na-Fe@C-pellet experienced severe aggregation during the CO₂ hydrogenation process with the Fe-based nanoparticles evolved into much larger than 100 nm in particle size (Fig. S9), while the Fe-based nanoparticle size in the spent Na-Fe@C-3D-spi was still maintained around 100 nm, which is close to that in the fresh catalyst (Fig. 11d and Fig. S3). And the Na and Fe elements in the spent Na-Fe@C-3D-spi were homogeneously dispersed on the carbon substrate as shown in the scanning transmission electron microscopy (STEM) elemental mapping images (Fig. 11e). It is reasonable to clarify that the active sites aggregation is responsible for the deactivation of Na-Fe@C-pellet. Furthermore, severe carbon deposition also occurred on the spent Na-Fe@C-pellet with the Raman peak intensity ratio (I_D/I_G) of disordered carbon (D band at around 1360 cm⁻¹) to graphitic carbon (G band at around 1600 cm⁻¹) was as high as 1.38 (Fig. S10), which is much higher than that of the fresh catalyst (I_D/I_G = 0.64) and the spent Na-Fe@C-3D-spi (I_D/I_G = 0.91). As we know, for the thermal-catalytic reaction, the uncontrollable heat-

transfer in the catalyst bed usually brings severe catalyst deactivation due to the active site aggregation and carbon deposition phenomena. For the Na-Fe@C-pellet with a densely packed configuration and weaker heat-transfer effect, the reaction heat from the exothermic FTS of carbon-chain propagation undoubtedly led to the formation of several hot spots in the catalyst bed. Even though the sluggish heat-transfer process and hot spots in Na-Fe@C-pellet boost the endothermic RWGS and carburization processes as reflected by the sharply increased CO₂ conversion rate and decreased CO selectivity at the initial stage of reaction, the facilitated active sites aggregation and carbon deposition inevitably resulted in the shortening of catalyst durability. Interestingly, benefiting from the facile heat-transfer effect as confirmed by the CFD simulation of the heat-transfer effect (Fig. 6j-l), Na-Fe@C-3D-spi monolithic catalyst delivered excellent catalyst durability in CO₂ hydrogenation.

The 3D printing technology-induced mass transfer enhancement effect can also be spread into the oriented conversion of syngas to targeted products (Fig. S11 and Table S8). The catalytic performance variation trends in syngas conversion catalyzed by Na-Fe@C-pellet and 3D-printed catalysts were similar to that in CO₂ hydrogenation reactions, especially in the selectivity and STY of light olefins. Benefiting from the facilitated desorption of olefins and timely termination of carbon-chain growth stem from the excellent mass-transfer process, the most outstanding light olefins selectivity (43.0%) and STY (421.7 g_{CH₂} kg_{cat}⁻¹ h⁻¹) were achieved from the Na-Fe@C-3D-spi catalyst. More importantly, this oriented synthesis tailoring strategy that based on 3D-printing technology is promising to extend into other catalytic systems, such as biomass conversion and fine chemicals synthesis.

3.3. More in-depth mechanism insights of 3D printing technology enhanced light olefins synthesis

It is understandable that the 3D printing enhanced mass-transfer effect could facilitate the desorption of reaction intermediates and alkenes from the catalytic interfaces, therefore boosting the synthesis of light olefins by avoiding the excessive carbon-chain growth and over-hydrogenation phenomena. Basically, the different mass-transfer effects vary the coverage of intermediates on the catalytic interface due to the different reaction behaviors. For example, on the Fe₅C₂ active site, the immediate mass-transfer effect (in Na-Fe@C-3D-str and Na-Fe@C-3D-spi samples) not only facilitates the vacation of catalytic active sites for the consumption of -C_mH_n * intermediates via C-C coupling step but also accelerates the desorption of products that formed from the carbon-chain termination of -C_mH_n *, which synergistically affords low coverage of -C_mH_n * intermediates on the Fe₅C₂ catalytic interface. More in-depth, the unique electronic property of the catalytic interface endowed by different coverage degrees of -C_mH_n * intermediates might be the original cause of the variation of reaction performance[34]. Herein, we employed density functional theory (DFT) simulations to clarify the reaction mechanism more detailed. The theoretical Fe₅C₂(510) models with different numbers of intermediates (n = 0, 1, 2, 4, 5, or 6, and carbene -CH₂ * as the representative intermediate) adsorbed on them were built to describe the mass-transfer effect-derived different catalytic interfaces (Fig. S12). The differential charge density plots confirmed that the electrophilic -CH₂ * species guaranteed the electron-deficient property of the Fe₅C₂(510) catalytic interface, and the Bader charge analysis (Fig. 12a) quantified that the number of the contributing electrons from Fe species follows the sequence of Fe₅C₂(510) - 6CH₂ * (2.9 e⁻) > Fe₅C₂(510) - 5CH₂ * (2.3 e⁻) > Fe₅C₂(510) - 4CH₂ * (2.0 e⁻) > Fe₅C₂(510) - 2CH₂ * (1.0 e⁻) > Fe₅C₂(510)-CH₂ * (0.4 e⁻) > Fe₅C₂(510) (0 e⁻). Obviously, the electron density in Fe species of Fe₅C₂(510) decreased with the increase of intermediates on the catalytic interface.

As illustrated in Fig. 12b, Fig. S13-S15, and Table S9, the energy profiles, the energetically favorable configurations, and the corresponding energy data of the elementary steps, including C-C coupling

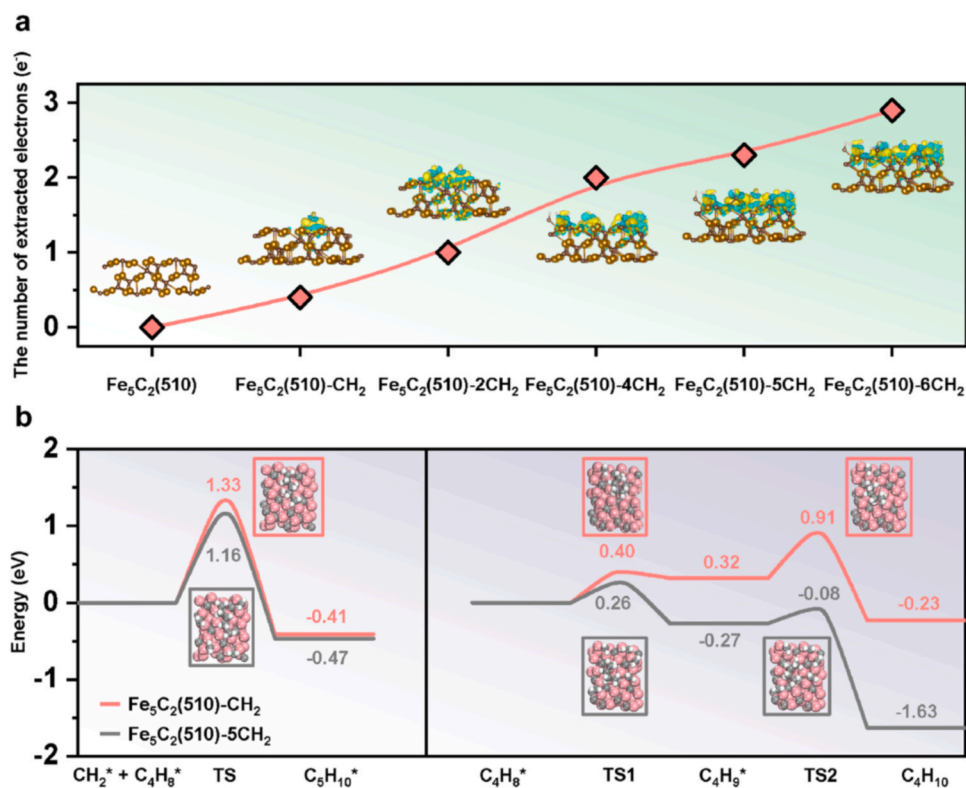


Fig. 12. (a) The number of extracted electrons from the Fe species in Fe₅C₂(510), Fe₅C₂(510)-CH₂, Fe₅C₂(510)-2CH₂, Fe₅C₂(510)-4CH₂, Fe₅C₂(510)-5CH₂, and Fe₅C₂(510)-6CH₂ models, insets are the differential charge density plots of the corresponding models, the yellow and cyan colors represent the accumulation and depletion electrons, respectively. (b) Energy profiles of C-C coupling between -CH₂* and -C₄H₈* and hydrogenation of -C₄H₈*, insets are the molecule models of the transition states (TS). Fe atoms in pink, C atoms in grey, and H atoms in white.

between -C₄H₈* and -CH₂* for carbon chain growth and stepwise hydrogenation of unsaturated 1-butene (1-C₄H₈) to n-C₄H₁₀, on different models [with Fe₅C₂(510)-5CH₂* and Fe₅C₂(510)-CH₂* represent the high and low intermediate coverages, respectively] were plotted and calculated according to the theoretical simulations. For the Fe₅C₂(510)-CH₂* model with low intermediate coverage, a higher energy barrier of 1.33 eV was needed to complete the C-C coupling step between -C₄H₈* and -CH₂* compared to that on Fe₅C₂(510)-5CH₂* models (1.16 eV), which confirmed that the enhanced mass-transfer effect and low intermediate coverage could suppress the excessive carbon-chain growth and guarantee the high selectivity of light hydrocarbons (Fig. 12b, Fig. S13, and Table S9). Furthermore, the adsorption energy of unsaturated olefin 1-C₄H₈ on Fe₅C₂(510)-CH₂* (-0.39 eV) was weaker than that on Fe₅C₂(510)-5CH₂* (-0.49 eV), indicating that the low intermediates coverage given by fast mass-transfer effect could promote the desorption of olefins and avoid the undesirable over-hydrogenation reaction (Fig. S14). Subsequently, the energy barriers of unsaturated 1-C₄H₈ hydrogenation into normal alkane n-C₄H₁₀ on different models were computed (Fig. 12b, Fig. S15, and Table S9). We found that Fe₅C₂(510)-CH₂* should climb high energy barriers of 0.40 and 0.91 eV to accomplish the stepwise 1-C₄H₈ hydrogenation processes, whereas only 0.26 and 0.08 eV were needed on Fe₅C₂(510)-5CH₂*. Therefore, the electron-rich catalytic interface with low carbene intermediate coverage was favorable for olefins synthesis due to the sluggish over-hydrogenation process on it. The DFT calculations further verified that the low intermediate coverage and electron-deficient catalytic interface endowed by the enhanced mass-transfer effect boosted the light olefins synthesis by synergistically suppressing the excessive carbon-chain growth and over-hydrogenation of the re-adsorbed olefins.

4. Conclusions

In summary, we ingeniously optimized the mass/heat transfer architectures of the monolithic catalysts via 3D printing strategy. The Fe-based CO₂ hydrogenation catalyst with spiral channels exhibited

extremely high yield of light olefins and excellent catalyst lifetime. The mass-transfer and molecular-level reaction mechanism simulations verified that the low intermediates coverage on catalytic interface endowed by outstanding mass-transfer effect was beneficial for light olefins synthesis by avoiding the undesirable over-hydrogenation and excessive carbon-chain growth. Furthermore, the unique heat-transfer effect guaranteed the long-term stability of the monolithic catalysts by eliminating the hot spots in the reactor bed. This 3D printing enhanced mass/heat-transfer strategy not only narrows the product distribution of CO₂ hydrogenation on Fe-based catalysts but also provides an ideal catalyst tailoring means that can apply into other catalytic systems for targeted synthesis.

CRedit authorship contribution statement

Y.W., T.N., and M.B.W. designed this study, analyzed the data, and wrote the paper. S.L., H.Y., P.D., and M.J.L. performed most of the experiments and characterization. M.L. and C.Z. performed the simulations. W.W., J.C., X.F., and H.H. performed part of the characterization and gave valuable suggestions. M.Q.W., T.X., T.L. and Q.L. provided helpful discussion and gave valuable suggestions.

Declaration of Competing Interest

The authors declare that they have no known competing financial interests or personal relationships that could have appeared to influence the work reported in this paper.

Data Availability

Data will be made available on request.

Acknowledgement

Funding: This work was financially supported by the National Nature

Science Foundation of China (22108310), the Shandong Province Key Research Program (Major Scientific and Technological Innovation Project, 2020CXGC010402), the Science and Technology Innovation Project of the Shandong Energy Group Co., Ltd. (SNKJ2021BJ04, SNKJ2023A03), the Foundation of State Key Laboratory of High-efficiency Utilization of Coal and Green Chemical Engineering (2022-KF-75). We also appreciate the financial aid from the New Energy and Industrial Technology Development Organization (NEDO) of Japan, and the research programs from Toyo Tire Co., Ltd. and YKK Co., Ltd. supported this work.

Appendix A. Supporting information

Supplementary data associated with this article can be found in the online version at [doi:10.1016/j.apcatb.2023.123211](https://doi.org/10.1016/j.apcatb.2023.123211).

References

- [1] J. Wei, R. Yao, Y. Han, Q. Ge, J. Sun, Towards the development of the emerging process of CO₂ heterogeneous hydrogenation into high-value unsaturated heavy hydrocarbons, *Chem. Soc. Rev.* 50 (2021) 10764–10805, <https://doi.org/10.1039/D1CS00260K>.
- [2] D.R. Feldman, W.D. Collins, P.J. Gero, M.S. Torn, E.J. Mlawer, T.R. Shippert, Observational determination of surface radiative forcing by CO₂ from 2000 to 2010, *Nature* 519 (2015) 339–343, <https://doi.org/10.1038/nature14240>.
- [3] B.M. Tackett, E. Gomez, J.G. Chen, Net reduction of CO₂ via its thermocatalytic and electrocatalytic transformation reactions in standard and hybrid processes, *Nat. Catal.* 2 (2019) 381–386, <https://doi.org/10.1038/s41929-019-0266-y>.
- [4] L. Zhang, Z.-J. Zhao, J. Gong, Nanostructured materials for heterogeneous electrocatalytic CO₂ reduction and their related reaction mechanisms, *Angew. Chem. Int. Ed.* 56 (2017) 11326–11353, <https://doi.org/10.1002/anie.201612214>.
- [5] A. Álvarez, A. Bansode, A. Urakawa, A.V. Bavykina, T.A. Wezendonk, M. Makkee, J. Gascon, F. Kapteijn, Challenges in the greener production of formates/formic acid, methanol, and DME by heterogeneously catalyzed CO₂ hydrogenation processes, *Chem. Rev.* 117 (2017) 9804–9838, <https://doi.org/10.1021/acs.chemrev.6b00816>.
- [6] W. Zhou, K. Cheng, J. Kang, C. Zhou, V. Subramanian, Q. Zhang, Y. Wang, New horizon in C1 chemistry: breaking the selectivity limitation in transformation of syngas and hydrogenation of CO₂ into hydrocarbon chemicals and fuels, *Chem. Soc. Rev.* 48 (2019) 3193–3228, <https://doi.org/10.1039/C8CS00502H>.
- [7] Y. Wang, X. Gao, M. Wu, N. Tsubaki, Thermocatalytic hydrogenation of CO₂ into aromatics by tailor-made catalysts: Recent advancements and perspectives, *EcoMat* 3 (2021), e12080, <https://doi.org/10.1002/eom.2.12080>.
- [8] B. Zhao, M. Sun, F. Chen, Y. Shi, Y. Yu, X. Li, B. Zhang, Unveiling the activity origin of iron nitride as catalytic material for efficient hydrogenation of CO₂ to C₂₊ hydrocarbons, *Angew. Chem. Int. Ed.* 133 (2021) 4546–4550, <https://doi.org/10.1002/ange.202015017>.
- [9] J. Wei, J. Sun, Z. Wen, C. Fang, Q. Ge, H. Xu, New insights into the effect of sodium on Fe₃O₄-based nanocatalysts for CO₂ hydrogenation to light olefins, *Catal. Sci. Technol.* 6 (2016) 4786–4793, <https://doi.org/10.1039/C6CY00160B>.
- [10] J. Wei, Q. Ge, R. Yao, Z. Wen, C. Fang, L. Guo, H. Xu, J. Sun, Directly converting CO₂ into a gasoline fuel, *Nat. Commun.* 8 (2017) 15174, <https://doi.org/10.1038/ncomms15174>.
- [11] P. Gao, S. Dang, S. Li, X. Bu, Z. Liu, M. Qiu, C. Yang, H. Wang, L. Zhong, Y. Han, Q. Liu, W. Wei, Y. Sun, Direct production of lower olefins from CO₂ conversion via bifunctional catalysis, *ACS Catal.* 8 (2018) 571–578, <https://doi.org/10.1021/acscatal.7b02649>.
- [12] Y. Wang, L. Tan, M. Tan, P. Zhang, Y. Fang, Y. Yoneyama, G. Yang, N. Tsubaki, Rationally designing bifunctional catalysts as an efficient strategy to boost CO₂ hydrogenation producing value-added aromatics, *ACS Catal.* 9 (2019) 895–901, <https://doi.org/10.1021/acscatal.8b01344>.
- [13] Z. Li, Y. Qu, J. Wang, H. Liu, M. Li, S. Miao, C. Li, Highly selective conversion of carbon dioxide to aromatics over tandem catalysts, *Joule* 3 (2019) 570–583, <https://doi.org/10.1016/j.joule.2018.10.027>.
- [14] Y. Wang, K. Wang, B. Zhang, X. Peng, X. Gao, G. Yang, H. Hu, M. Wu, N. Tsubaki, Direct conversion of CO₂ to ethanol boosted by intimacy-sensitive multifunctional catalysts, *ACS Catal.* 11 (2021) 11742–11753, <https://doi.org/10.1021/acscatal.1c01504>.
- [15] J. Liu, Y. Song, X. Guo, C. Song, X. Guo, Recent advances in application of iron-based catalysts for CO_x hydrogenation to value-added hydrocarbons, *Chinese, J. Catal.* 43 (2022) 731–754, [https://doi.org/10.1016/S1872-2067\(21\)63802-0](https://doi.org/10.1016/S1872-2067(21)63802-0).
- [16] Z. Li, J. Liu, R. Shi, G.I.N. Waterhouse, X.-D. Wen, T. Zhang, Fe-based catalysts for the direct photoreduction of CO₂ to value-added hydrocarbons, *Adv. Energy Mater.* 12 (2022) 2200475, <https://doi.org/10.1002/aenm.202200475>.
- [17] L. Guo, J. Sun, Q. Ge, N. Tsubaki, Recent advances in direct catalytic hydrogenation of carbon dioxide to valuable C₂₊ hydrocarbons, *J. Mater. Chem. A* 6 (2018) 23244–23262, <https://doi.org/10.1039/c8ta05377d>.
- [18] J. Zhu, P. Wang, X. Zhang, G. Zhang, R. Li, W. Li, T.P. Senftle, W. Liu, J. Wang, Y. Wang, A. Zhang, Q. Fu, C. Song, X. Guo, Dynamic structural evolution of iron catalysts involving competitive oxidation and carburization during CO₂ hydrogenation, *Sci. Adv.* 8 (2022) eabm3629, <https://doi.org/10.1126/sciadv.abm3629>.
- [19] Q. Yang, V.A. Kondratenko, S.A. Petrov, D.E. Doronkin, E. Saraçi, H. Lund, A. Arinchein, R. Kraehnert, A.S. Skrynnik, A.A. Matvienko, E.V. Kondratenko, Identifying performance descriptors in CO₂ hydrogenation over iron-based catalysts promoted with alkali metals, *Angew. Chem. Int. Ed.* 61 (2022), e202116517, <https://doi.org/10.1002/anie.202116517>.
- [20] P. Zhai, C. Xu, R. Gao, X. Liu, M. Li, W. Li, X. Fu, C. Jia, J. Xie, M. Zhao, X. Wang, Y.-W. Li, Q. Zhang, X.-D. Wen, D. Ma, Highly tunable selectivity for syngas-derived alkenes over zinc and sodium-modulated Fe₃C₂ catalyst, *Angew. Chem. Int. Ed.* 128 (2016) 10056–10061, <https://doi.org/10.1002/ange.201603556>.
- [21] A. Ramirez, L. Gevers, A. Bavykina, S. Ould-Chikh, J. Gascon, Metal organic framework-derived iron catalysts for the direct hydrogenation of CO₂ to short chain olefins, *ACS Catal.* 8 (2018) 9174–9182, <https://doi.org/10.1021/acscatal.8b02892>.
- [22] Y. Wang, S. Kazumi, W. Gao, X. Gao, H. Li, X. Guo, Y. Yoneyama, G. Yang, N. Tsubaki, Direct conversion of CO₂ to aromatics with high yield via a modified Fischer-Tropsch synthesis pathway, *Appl. Catal. B Environ.* 269 (2020), 118792, <https://doi.org/10.1016/j.apcatb.2020.118792>.
- [23] B. Yao, T. Xiao, O.A. Makgae, X. Jie, S. Gonzalez-Cortes, S. Guan, A.I. Kirkland, J. R. Dilworth, H.A. Al-Megren, S.M. Alshihri, P.J. Dobson, G.P. Owen, J.M. Thomas, P.P. Edwards, Transforming carbon dioxide into jet fuel using an organic combustion-synthesized Fe-Mn-K catalyst, *Nat. Commun.* 11 (2020) 6395, <https://doi.org/10.1038/s41467-020-20214-z>.
- [24] Z. Zhang, G. Huang, X. Tang, H. Yin, J. Kang, Q. Zhang, Y. Wang, Zn and Na promoted Fe catalysts for sustainable production of high-valued olefins by CO₂ hydrogenation, *Fuel* 309 (2022), 122105, <https://doi.org/10.1016/j.fuel.2021.122105>.
- [25] L. Guo, X. Gao, W. Gao, H. Wu, X. Wang, S. Sun, Y. Wei, Y. Kugue, X. Guo, J. Sun, N. Tsubaki, High-yield production of liquid fuels in CO₂ hydrogenation on a zeolite-free Fe-based catalyst, *Chem. Sci.* 14 (2023) 171–178, <https://doi.org/10.1039/D2SC05047A>.
- [26] C. Zhang, C. Cao, Y. Zhang, X. Liu, J. Xu, M. Zhu, W. Tu, Y.-F. Han, Unraveling the role of zinc on bimetallic Fe₃C₂-ZnO catalysts for highly selective carbon dioxide hydrogenation to high carbon α -olefins, *ACS Catal.* 11 (2021) 2121–2133, <https://doi.org/10.1021/acscatal.0c04627>.
- [27] Z. Li, W. Wu, M. Wang, Y. Wang, X. Ma, L. Luo, Y. Chen, K. Fan, Y. Pan, H. Li, J. Zeng, Ambient-pressure hydrogenation of CO₂ into long-chain olefins, *Nat. Commun.* 13 (2022) 2396, <https://doi.org/10.1038/s41467-022-09971-5>.
- [28] E. Iglesia, S.C. Reyes, R.J. Madon, Transport-enhanced α -olefin readsorption pathways in Ru-catalyzed hydrocarbon synthesis, *J. Catal.* 129 (1991) 238–256, [https://doi.org/10.1016/0021-9517\(91\)90027-2](https://doi.org/10.1016/0021-9517(91)90027-2).
- [29] N. Duyckaerts, M. Bartsch, I.-T. Trotsu, N. Pfänder, A. Lorke, F. Schüth, G. Prieto, Intermediate product regulation in tandem solid catalysts with multimodal porosity for high-yield synthetic fuel production, *Angew. Chem. Int. Ed.* 56 (2017) 11480–11484, <https://doi.org/10.1002/anie.201705714>.
- [30] C. Zhu, D.P. Gamliel, J.A. Valla, G.M. Bolas, Fischer-Tropsch synthesis in monolith catalysts coated with hierarchical ZSM-5, *Appl. Catal. B Environ.* 284 (2021), 119719, <https://doi.org/10.1016/j.apcatb.2020.119719>.
- [31] T. Li, X. Wen, Y.-W. Li, H. Jiao, Mechanistic insight into CO activation, methanation and C-C bond formation from coverage dependent CO hydrogenation on Fe(110), *Surf. Sci.* 689 (2019), 121456, <https://doi.org/10.1016/j.susc.2019.121456>.
- [32] P. Zhai, Y. Li, M. Wang, J. Liu, Z. Cao, J. Zhang, Y. Xu, X. Liu, Y.-W. Li, Q. Zhu, D. Xiao, X.-D. Wen, D. Ma, Development of direct conversion of syngas to unsaturated hydrocarbons based on Fischer-Tropsch route, *Chem* 7 (2021) 3027–3051, <https://doi.org/10.1016/j.chempr.2021.08.019>.
- [33] Y. Zhang, X. Yang, X. Yang, H. Duan, H. Qi, Y. Su, B. Liang, H. Tao, B. Liu, D. Chen, X. Su, Y. Huang, T. Zhang, Tuning reactivity of Fischer-Tropsch synthesis by regulating TiO_x overlayer over Ru/TiO_x nanocatalysts, *Nat. Commun.* 11 (2020) 3185, <https://doi.org/10.1038/s41467-020-17044-4>.
- [34] R. Zhang, C. Wei, D. Li, Z. Jiang, B. Wang, L. Ling, M. Fan, The new role of surface adsorbed CH_x (x = 1–3) intermediates as a co-adsorbed promoter in self-promoting syngas conversion to form CH_x intermediates and C₂ oxygenates on the Rh-doped Cu catalyst, *J. Catal.* 377 (2019) 1–12, <https://doi.org/10.1016/j.jcat.2019.07.019>.
- [35] N.S. Govender, F.G. Botes, M.H.J.M. de Croon, J.C. Schouten, Mechanistic pathway for C₂₊ hydrocarbons over an Fe/K catalyst, *J. Catal.* 312 (2014) 98–107, <https://doi.org/10.1016/j.jcat.2014.01.012>.
- [36] Y. Jiao, H. Ma, P. Ren, T. Li, Y.-W. Li, X.-D. Wen, H. Jiao, Exploring coverage-dependent chain-growth mechanisms on Ru(111) for Fischer-Tropsch synthesis, *Catal. Sci. Technol.* 13 (2023) 437–456, <https://doi.org/10.1039/D2CY01279K>.
- [37] K.S. Kshetrimayum, I. Jung, J. Na, S. Park, Y. Lee, S. Park, C.-J. Lee, C. Han, CFD simulation of microchannel reactor block for Fischer-Tropsch synthesis: effect of coolant type and wall boiling condition on reactor temperature, *Ind. Eng. Chem. Res.* 55 (2016) 543–554, <https://doi.org/10.1021/acs.iecr.5b03283>.
- [38] J. Shen, Y.-C. Li, W.H. Ho, X. Liu, D. Hildebrandt, Experimental and simulation study of the temperature distribution in a bench-scale fixed bed Fischer-Tropsch reactor, *AIChE J.* 67 (2021), e17145, <https://doi.org/10.1002/aic.17145>.
- [39] Q. Wei, H. Li, G. Liu, Y. He, Y. Wang, Y.E. Tan, D. Wang, X. Peng, G. Yang, N. Tsubaki, Metal 3D printing technology for functional integration of catalytic system, *Nat. Commun.* 11 (2020) 4098, <https://doi.org/10.1038/s41467-020-17941-8>.
- [40] C. Zhu, Z. Qi, V.A. Beck, M. Luneau, J. Lattimer, W. Chen, M.A. Worsley, J. Ye, E. B. Duoss, C.M. Spadaccini, C.M. Friend, J. Biener, Toward digitally controlled

- catalyst architectures: Hierarchical nanoporous gold via 3D printing, *Sci. Adv.* 4 (2018) eaas9459, <https://doi.org/10.1126/sciadv.aas9459>.
- [41] P.J. Kitson, S. Glatzel, W. Chen, C.-G. Lin, Y.-F. Song, L. Cronin, 3D printing of versatile reactionware for chemical synthesis, *Nat. Protoc.* 11 (2016) 920–936, <https://doi.org/10.1038/nprot.2016.041>.
- [42] M.D. Symes, P.J. Kitson, J. Yan, C.J. Richmond, G.J.T. Cooper, R.W. Bowman, T. Vilbrandt, L. Cronin, Integrated 3D-printed reactionware for chemical synthesis and analysis, *Nat. Chem.* 4 (2012) 349–354, <https://doi.org/10.1038/nchem.1313>.
- [43] V.G. Rocha, E. Saiz, I.S. Tirichenko, E. García-Tuñón, Direct ink writing advances in multi-material structures for a sustainable future, *J. Mater. Chem. A* 8 (2020) 15646–15657, <https://doi.org/10.1039/D0TA04181E>.
- [44] C. Parra-Cabrera, C. Achille, S. Kuhn, R. Ameloot, 3D printing in chemical engineering and catalytic technology: structured catalysts, mixers and reactors, *Chem. Soc. Rev.* 47 (2018) 209–230, <https://doi.org/10.1039/C7CS00631D>.
- [45] S. Hock, C. Rein, M. Rose, 3D-printed acidic monolithic catalysts for liquid-phase catalysis with enhanced mass transfer properties, *ChemCatChem* 14 (2022), e202101947, <https://doi.org/10.1002/cctc.202101947>.
- [46] S. Rossi, R. Porta, D. Brenna, A. Puglisi, M. Benaglia, Stereoselective catalytic synthesis of active pharmaceutical ingredients in homemade 3D-printed mesoreactors, *Angew. Chem. Int. Ed.* 129 (2017) 4354–4358, <https://doi.org/10.1002/ange.201612192>.
- [47] X. Zhou, C.-J. Liu, Three-dimensional printing for catalytic applications: current status and perspectives, *Adv. Funct. Mater.* 27 (2017) 1701134, <https://doi.org/10.1002/adfm.201701134>.
- [48] G. Kresse, J. Furthmüller, Efficient iterative schemes for ab initio total-energy calculations using a plane-wave basis set, *Phys. Rev. B* 54 (1996) 11169–11186, <https://doi.org/10.1103/PhysRevB.54.11169>.
- [49] G. Kresse, J. Furthmüller, Efficiency of ab-initio total energy calculations for metals and semiconductors using a plane-wave basis set, *Comput. Mater. Sci.* 6 (1996) 15–50, [https://doi.org/10.1016/0927-0256\(96\)00008-0](https://doi.org/10.1016/0927-0256(96)00008-0).
- [50] J.P. Perdew, K. Burke, M. Ernzerhof, Generalized gradient approximation made simple, *Phys. Rev. Lett.* 77 (1996) 3865–3868, <https://doi.org/10.1103/PhysRevLett.77.3865>.
- [51] J.A. White, D.M. Bird, Implementation of gradient-corrected exchange-correlation potentials in Car-Parrinello total-energy calculations, *Phys. Rev. B* 50 (1994) 4954–4957, <https://doi.org/10.1103/PhysRevB.50.4954>.
- [52] G. Henkelman, H. Jónsson, Improved tangent estimate in the nudged elastic band method for finding minimum energy paths and saddle points, *J. Chem. Phys.* 113 (2000) 9978–9985, <https://doi.org/10.1063/1.1323224>.
- [53] G. Henkelman, H. Jónsson, A dimer method for finding saddle points on high dimensional potential surfaces using only first, *J. Chem. Phys.* 111 (1999) 7010–7022, <https://doi.org/10.1063/1.480097>.
- [54] G. Henkelman, A. Arnaldsson, H. Jónsson, A fast and robust algorithm for Bader decomposition of charge density, *Comput. Mater. Sci.* 36 (2006) 354–360, <https://doi.org/10.1016/j.commatsci.2005.04.010>.
- [55] E. Sanville, S.D. Kenny, R. Smith, G. Henkelman, Improved grid-based algorithm for Bader charge allocation, *J. Comput. Chem.* 28 (2007) 899–908, <https://doi.org/10.1002/jcc.20575>.
- [56] V. Wang, N. Xu, J.-C. Liu, G. Tang, W.-T. Geng, VASPKIT: A user-friendly interface facilitating high-throughput computing and analysis using VASP code, *Comput. Phys. Commun.* 267 (2021), 108033, <https://doi.org/10.1016/j.cpc.2021.108033>.
- [57] M. Zhang, J. Ren, Y. Yu, Insights into the hydrogen coverage effect and the mechanism of Fischer–Tropsch to olefins process on Fe₅C₂ (510), *ACS Catal.* 10 (2020) 689–701, <https://doi.org/10.1021/acscatal.9b03639>.
- [58] Y. Jiang, Z. Xu, T. Huang, Y. Liu, F. Guo, J. Xi, W. Gao, C. Gao, Direct 3D printing of ultralight graphene oxide aerogel microlattices, *Adv. Funct. Mater.* 28 (2018) 1707024, <https://doi.org/10.1002/adfm.201707024>.
- [59] L. Yu, Z. Fan, Y. Shao, Z. Tian, J. Sun, Z. Liu, Versatile N-doped MXene ink for printed electrochemical energy storage application, *Adv. Energy Mater.* 9 (2019) 1901839, <https://doi.org/10.1002/aenm.201901839>.
- [60] Z. Fan, C. Wei, L. Yu, Z. Xia, J. Cai, Z. Tian, G. Zou, S.X. Dou, J. Sun, 3D printing of porous nitrogen-doped Ti₃C₂ MXene scaffolds for high-performance sodium-ion hybrid capacitors, *ACS Nano* 14 (2020) 867–876.
- [61] D. Kong, Y. Wang, S. Huang, B. Zhang, Y.V. Lim, G.J. Sim, P. Valdivia, y Alvarado, Q. Ge, H.Y. Yang, 3D printed compressible quasi-solid-state nickel–iron battery, *ACS Nano* 14 (2020) 9675–9686.
- [62] V. Navarro, M.A. van Spronsen, J.W.M. Frenken, In situ observation of self-assembled hydrocarbon Fischer–Tropsch products on a cobalt catalyst, *Nat. Chem.* 8 (2016) 929–934, <https://doi.org/10.1038/nchem.2613>.
- [63] W. Fang, C. Wang, Z. Liu, L. Wang, L. Liu, H. Li, S. Xu, A. Zheng, X. Qin, L. Liu, F.-S. Xiao, Physical mixing of a catalyst and a hydrophobic polymer promotes CO hydrogenation through dehydration, *Science* 377 (2022) 406–410, <https://doi.org/10.1126/science.abo0356>.
- [64] Y. Xu, X. Li, J. Gao, J. Wang, G. Ma, X. Wen, Y. Yang, Y. Li, M. Ding, A hydrophobic FeMn/Si catalyst increases olefins from syngas by suppressing C1 by-products, *Science* 371 (2021) 610–613, <https://doi.org/10.1126/science.abb3649>.
- [65] L. Guo, J. Sun, X. Ji, J. Wei, Z. Wen, R. Yao, H. Xu, Q. Ge, Directly converting carbon dioxide to linear α -olefins on bio-promoted catalysts, *Commun. Chem.* 1 (2018) 11, <https://doi.org/10.1038/s42004-018-0012-4>.